

# Supplementary Material

Yan Lu<sup>1,†,\*</sup> Xinzhu Ma<sup>1,\*</sup> Lei Yang<sup>2</sup> Tianzhu Zhang<sup>3</sup>  
 Yating Liu<sup>4</sup> Qi Chu<sup>3,✉</sup> Junjie Yan<sup>2</sup> Wanli Ouyang<sup>1</sup>

<sup>1</sup>The University of Sydney, SenseTime Computer Vision Group <sup>2</sup>Sensetime Group Limited  
<sup>3</sup>School of Information Science and Technology, University of Science and Technology of China

<sup>4</sup>School of Data Science, University of Science and Technology of China

{yan.lul, xinzhu.ma, wanli.ouyang}@sydney.edu.au {yanglei, yanjunjie}@sensetime.com  
 {tzzhang, qchu}@ustc.edu.cn liuyat@mail.ustc.edu.cn

Table 1: **AP<sub>11</sub> Performance of the Car category on the KITTI validation set.** We highlight the best results in **bold**.

Method	3D@IoU=0.7			BEV@IoU=0.7			3D@IoU=0.5			BEV@IoU=0.5		
	Easy	Mod.	Hard	Easy	Mod.	Hard	Easy	Mod.	Hard	Easy	Mod.	Hard
Mono3D [2]	2.53	2.31	2.31	5.22	5.19	4.13	-	-	-	-	-	-
OFTNet [13]	4.07	3.27	3.29	11.06	8.79	8.91	-	-	-	-	-	-
Deep3DBox [11]	5.85	4.19	3.84	9.99	7.71	5.30	27.04	20.55	15.88	30.02	23.77	18.83
FQNet [8]	5.98	5.50	4.75	9.50	8.02	7.71	28.16	28.16	28.16	32.57	24.60	21.25
Mono3D++ [5]	10.60	7.90	5.70	16.70	11.50	10.10	42.00	29.80	24.20	46.70	34.30	28.10
GS3D [6]	13.46	10.97	10.38	-	-	-	32.15	29.89	29.89	-	-	-
MonoGRNet [12]	13.88	10.19	7.62	50.51	36.97	30.82	-	-	-	-	-	-
MonoDIS [14]	18.05	14.98	13.42	24.26	18.43	16.95	-	-	-	-	-	-
M3D-RPN [1]	20.27	17.06	15.21	25.94	21.18	21.18	48.96	39.57	33.01	53.35	39.60	31.76
RTM3D [7]	20.77	20.77	16.63	25.56	22.12	20.91	54.36	41.90	35.84	57.47	44.16	42.31
RARNet [9]+GS3D [6]	11.63	10.51	10.51	14.34	12.52	11.36	30.60	26.40	22.89	38.24	32.01	28.71
RARNet [9]+MonoGRNet [12]	13.84	10.11	7.59	24.84	19.27	16.20	50.27	36.67	30.53	53.91	39.45	32.84
RARNet [9]+M3D-RPN [1]	23.12	19.82	16.19	29.16	22.14	18.78	51.20	44.12	32.12	57.12	44.41	37.12
GUP Net (Ours)	<b>25.76</b>	<b>20.48</b>	<b>17.24</b>	<b>34.00</b>	<b>24.81</b>	<b>22.96</b>	<b>59.36</b>	<b>45.03</b>	<b>38.14</b>	<b>62.58</b>	<b>46.82</b>	<b>44.81</b>

## 0. Overview

In this supplementary material, we would introduce more details and experiments about our GUPNet. In section 1, we give more visualization results about our method, including 3D detection results and scores visualization. In section 2, we compare more state-of-the-art methods in the AP<sub>11</sub> setting. In section 3, we introduce more details of loss functions we use. In section 4, we introduce the normalized coordinate maps that we utilize in section 3.2 in the original paper. In section 5, we introduce a 3D data augmentation method that we propose and use in the original paper.

## 1. 3D detection visualization

We show some detection results of our method. We first estimate the 3D bounding boxes by our method, and then project the boxes on the image plane to draw them on

the scene image. The results are shown in Figure 1. We also give additional visualization of scores, we draw the 2D score  $p_{2d}$ , the depth score (3D scores conditioned on the 2D information)  $p_{3d|2d}$  and the final 3D scores  $p_{3d}$  in Figure 2, showing that both  $p_{2d}$  and  $p_{3d|2d}$  contribute to the final score and leading to better detection reliability.

## 2. Further Comparison

There are some works that do not report the newly released AP<sub>40</sub> metric on the KITTI validation dataset. So we do not compare them on the validation set in the original paper. Here, we show the further comparison under AP<sub>11</sub> metric on the validation set with the state-of-the-art methods in Table 1.

Under the AP<sub>11</sub> setting, our method gets the best competing performance whatever the IoU threshold is. Specifically, our method surpasses RAR-Net [9] by 2.64%/4.84% AP under the easy setting at 0.7 IoU threshold. And for the 0.5 IoU threshold, we also achieve 8.16% and 5.46% gains for 3D/BEV detection under the easy setting respectively.

<sup>†</sup>This work was done when Yan Lu was an intern at SenseTime.

<sup>\*</sup>Equal contribution.

<sup>✉</sup>Qi Chu is the corresponding author.



Figure 1: Projected 3D Detection results of our method. We use green, blue and red to indicate car, pedestrian and cyclist categories, respectively.





Figure 2: Visualization of different kinds of scores.

This shows the high-precision performance of our method.

### 3. Loss function details

In this section, we would describe more details about loss functions.

#### 3.1. 2D Detection loss function details

Our 2D detection module is built on the CenterNet [4]. Details can be seen in the original paper. The heatmap loss is defined as:

$$\begin{aligned} \mathcal{L}_{heatmap} &= \text{Focal}(Y, Y^{gt}) \\ &= \frac{-1}{WHC} \sum_{uv} \begin{cases} (1 - Y_{uv})^\alpha \log(Y_{uv}), & \text{if } Y_{uv}^{gt} = 1 \\ (1 - Y_{uv}^{gt})^\beta Y_{uv}^\alpha \log(1 - Y_{uv}), & \text{otherwise} \end{cases}, \end{aligned} \quad (1)$$

where  $Y$  represents the predicted heatmaps and  $Y^{gt}$  is the ground-truth heatmaps.

The 2D size loss function is defined as:

$$\mathcal{L}_{size2d} = -\frac{1}{N} \sum_{k=1}^N (|w_{2d}(k) - w_{2d}^{gt}(k)| + |h_{2d}(k) - h_{2d}^{gt}(k)|), \quad (2)$$

where  $N$  is the total ground-truth object number on the current batch. The  $w_{2d}^{gt}$  and  $h_{2d}^{gt}$  are ground-truth size of the  $k$ -th object.

The 2D offset loss function is:

$$\mathcal{L}_{offset2d} = \frac{1}{N} \sum_{k=1}^N (|\delta_{2d}^u(k) - \delta_{2d}^{u,gt}(k)| + |\delta_{2d}^v(k) - \delta_{2d}^{v,gt}(k)|). \quad (3)$$

The  $\delta_{2d}^{u,gt}(k)$  and  $\delta_{2d}^{v,gt}(k)$  are the ground-truth offsets of the  $k$ -th object.

#### 3.2. Basic 3D Detection loss function details

The basic 3D detection loss function of our method follows the MonoPair [3]. The angle prediction task aims to predict the alpha angle [11, 15], which is the relative rotation of the camera viewing angle. The original 360° angle range is split into 12 bins and each bin covers 30° range. Its loss function is the *MultiBin* loss [11]:

$$\mathcal{L}_{angle} = \mathcal{L}_{conf}(\theta, \theta^{gt}) + \mathcal{L}_{loc}(\theta, \theta^{gt}). \quad (4)$$

And for the the ROI 3D demension estimation, its loss function is:

$$\mathcal{L}_{size3d} = \mathcal{L}_{h3d} + |w_{3d} - w_{3d}^{gt}| + |l_{3d} - l_{3d}^{gt}|. \quad (5)$$

Table 2: Statistic of calibration on KITTI. The  $(c_u, c_v)$  is the principal point and  $f$  is the focal length. The sample number means the total sample number corresponding to each kind of calibration.

Set	$c_u$	$c_v$	$f$	sample number
train	600.3891	181.5122	718.3351	103
	604.0814	180.5066	707.0493	445
	609.5593	172.8540	721.5377	3164
val	600.3891	181.5122	718.3351	255
	604.0814	180.5066	707.0493	325
	607.1928	185.2157	718.8560	296
	609.5593	172.8540	721.5377	2893
test	601.8873	183.1104	707.0912	71
	604.0814	180.5066	707.0493	868
	609.5593	172.8540	721.5377	6579

Finally, the ROI based 3D offset loss function is:

$$\mathcal{L}_{offset3d} = |\delta_{3d}^u(k) - \delta_{3d}^{u,gt}(k)| + |\delta_{3d}^v(k) - \delta_{3d}^{v,gt}(k)|. \quad (6)$$

#### 4. Normalized Plane Coordinate Maps

For better 3D information estimation, we concatenate the coordinate maps with the original ROI feature maps as the final ROI feature representation. For the coordinate maps, we design a new normalized plane coordinate maps (In the original paper, we call this ‘normalized coordinate’) instead of the commonly used coordinate maps [10].

We first review a concept in the geometry topic: normalized homogeneous plane. Every 2D coordinate  $(u, v)$  can be represented in the homogeneous format  $(u, v, 1)$ . And this point can be re-project back to the 3D coordinate:

$$\begin{aligned} x^{np} &= (u - c_u)/f, \\ y^{np} &= (v - c_v)/f, \\ z^{np} &= 1. \end{aligned} \quad (7)$$

This re-project result can be interpreted as a 3D point whose depth is 1. The tuple  $(x^{np}, y^{np}, 1)$  is called the normalized plane coordinate in the 3D space.

We propose to use this normalized plane coordinate  $(x^{np}, y^{np})$  as our coordinate maps, called Normalized Plane Coordinate Maps (NPCM) in supplementary. For each point in the 2D bounding box, we sample them and resize them to the same size with the ROI features ( $7 \times 7$ ), and then compute their corresponding normalized plane coordinate values as the coordinate maps.

The motivation of this design is that the normalized plane coordinate introduces the calibration information to the model, which can reduce the gap between the 2D and

Table 3: Comparison with standard coordinate maps on the KITTI *validation* set for the car category.

	3D@IoU=0.7			BEV@ IoU=0.7		
	Easy	Mod.	Hard	Easy	Mod.	Hard
No CoordMaps	19.94	15.36	12.96	27.51	20.68	17.62
Standar CoordMaps [10]	20.73	15.79	13.26	28.16	21.05	18.08
NPCM (Ours)	<b>22.76</b>	<b>16.46</b>	<b>13.72</b>	<b>31.07</b>	<b>22.94</b>	<b>19.75</b>

3D and alleviate difficulty of the monocular 3D detection learning. Here, we give a qualitative analysis. The calibration represents the relationship between the 2D coordinate and the 3D one. And actually, to predict the information in the 3D coordinate, the monocular 3D detector has to learn this relationship, otherwise it cannot transfer the 2D information into the 3D coordinate system. The main reason is that the target of the monocular 3D detection is predicting object parameters in a **specific** 3D coordinate which is agnostic for the system given only a single image. Thus, it forces the model to fit the 2D-3D relationship (calibration). From this point of view, we can conclude that if the calibration is not fixed, the overall learning process would cause bias. But we find that, in the KITTI dataset, the calibration has slight changes. We statistic the calibration information on the KITTI and show it in Table 2. It can be seen that the calibration is not fixed in each set and even different in the different split. So we propose NPCM to cover this problem. The NPCM directly introduces the calibration information so that the model does not need to regress this relationship from the data. And when the calibration files change, the model still gets the accurate relation so it can focus more on the object estimation task. We compare our NPCM with the traditional coordinate. The results can be seen in Table 3, which shows that our method can achieve better performance.

#### 5. Calibration Flip Augmentation

Existing methods often use image flip as the augmentation method. They directly flip the image and the 3D information together. But we find that directly using flipped images to train monocular 3D detection models would cause learning bias for our model. So we propose a Calibration Data Augmentation to solve this problem. Note that **all** experiments in the original paper have utilized this augmentation strategy.

As shown in Figure 4, the original flip augmentation assumes that the 3D scene and 2D image flip simultaneously, which is equal to assume that the 2D and 3D symmetry axis are aligned with each other. But we find that this assumption is not accurate. We draw both 2D and 3D symmetry axis on the image plane in Figure 3. We can see that the two symmetry axis are not aligned with each other, which



Figure 3: 2D and 3D symmetry axis visualization. The green arrow is the 3D symmetry axis. And the blue line represents the 2D symmetry axis (Image center axis).

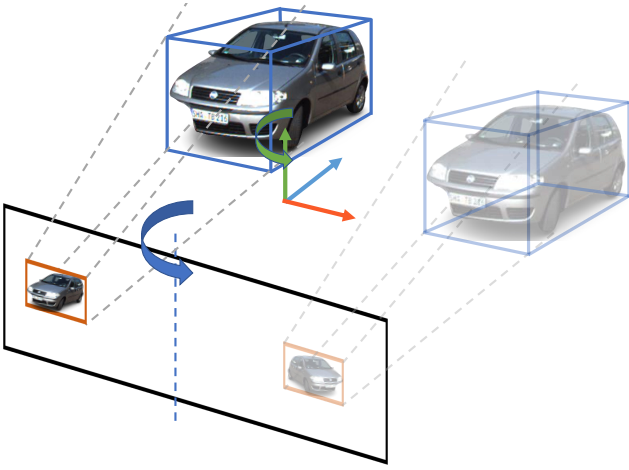


Figure 4: The motivation of the original image flip augmentation. The 2D and 3D coordinates are flip together.

means that the original assumption does not hold.

We give some further experiments of two views to prove that this misalignment would cause label noise:

**Image view: Flip in 3D→Project.** We first flip the 3D box along the 3D symmetry axis and project them on the 2D image plane and see the alignment situation with the flipped image. The results are shown in Figure 6. This means that the relationship between the flipped 3D coordinate and the flipped image plane has changed relative to the un-flipped one.

**3D view: Project→Flip in 2D→Backproject.** We also do similar experiments to show the misalignment in the 3D system view. We first project the 3D boxes to the image and flip the projected box along the 2D symmetry axis. This operation makes the flipped projected boxes and the image

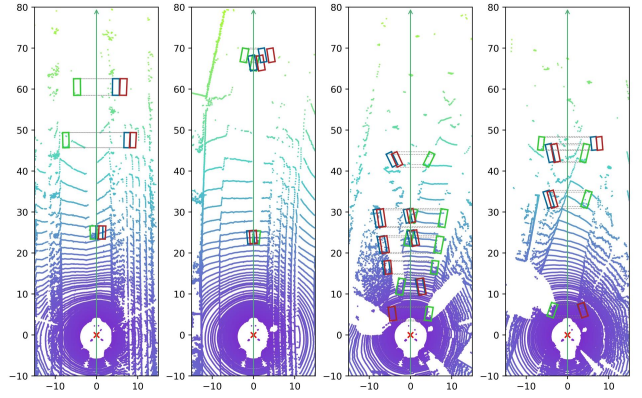


Figure 5: Birds-view examples for showing the misalignment in the 3D space. The blue boxes are flipped 3D boxes. The red boxes are generated by back projecting the 2D flipped projected boxes.

be aligned with each other. And then, we re-project these boxes back into the 3D space. The results are shown in Figure 5. We can find that they are not aligned with boxes flipped along the 3D symmetry axis.

These misalignment make the 2D and 3D relationship changes. For the traditional deep learning methods, it forces the model to fit this bias. And for the geometry methods, such as our GUP Net, it makes the geometry results not accurate and introduces the noise. Its influence on our model represents in two modules. The first one is the normalized plane coordinate maps (Eq. 7) and the second one is the GUP module (The projection pipeline requests the focal length parameter  $f$ ). So we propose the Calibration Flip Augmentation (CFA) to treat this problem. The overall pipeline is as follows: For each sample, we first flip the 2D



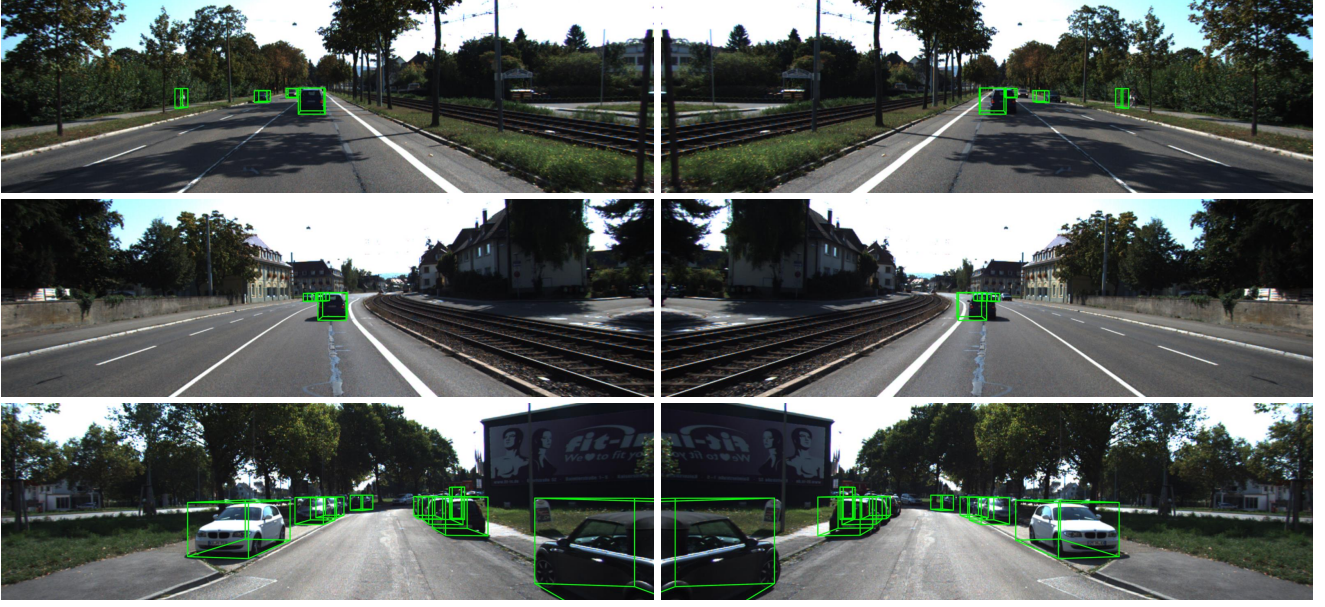


Figure 6: The misalignment of the original mage flip augmentation in the image view. The left column is the original image and the right column shows the flipped one. After flipping, we could see the bounding boxes have different degrees of bias. It is caused by the symmetry axis misalignment (Figure 3).

image and 3D bounding box. And then we compute a new set of calibration parameters based on these flipped pairs.

Before the flipping operation, we sample  $M$  3D points uniformly in the 3D coordinate and get their corresponding 2D points on the image. And then we flip the 2D points along the 2D image symmetry axis and the 3D points along the 3D symmetry axis. Now for these  $M$  point pairs. We use the least-squares method to solve the Perspective-N-Points (PNP) solution and compute the new calibration information:

$$\{c_u^{new}, c_v^{new}, f^{new}\} = \underset{c_u, c_v, f}{\operatorname{argmin}} e_{\text{PNP}},$$

$$e_{\text{PNP}} = \frac{1}{M} \sum_{i=0}^{M-1} \left\{ \begin{bmatrix} u_i \\ v_i \\ 1 \end{bmatrix} - \frac{1}{z_i} \begin{bmatrix} f & 0 & c_u \\ 0 & f & c_v \\ 0 & 0 & 1 \end{bmatrix} \begin{bmatrix} x_i \\ y_i \\ z_i \end{bmatrix} \right\}, \quad (8)$$

where  $[u_i, v_i]$  and  $[x_i, y_i, z_i]$  represent 2D and 3D point of the  $i$ -th flipped pair. This new calibration re-aligns the 2D and 3D relationships for the flipped pairs, which provides better results for our model. We present a comparison in Table 4. We set the model not using flipping augmentation as the comparison baseline, which can achieve 14.29% and 20.27% on the 3D and BEV Moderate settings. And we find that using the original flip would cause a large performance drop of about -2.46% and -3.45% on these two settings. It proves our argument that the original flipping changes the 2D-3D relationships which damages the ge-

Table 4: Comparison with different flip augmentation methods on the KITTI *validation* set for the car category.

	3D@IoU=0.7			BEV@ IoU=0.7		
	Easy	Mod.	Hard	Easy	Mod.	Hard
No flip	19.22	14.29	11.81	26.55	20.27	16.51
Direct flip	15.24	11.82	9.74	22.21	16.82	14.14
Flip with CFA (Ours)	<b>22.76</b>	<b>16.46</b>	<b>13.72</b>	<b>31.07</b>	<b>22.94</b>	<b>19.75</b>

ometry knowledge learned by the geometry-based methods. For our model, inaccurate 2D-3D relationships introduce bias coordinate maps and wrong projected depth, so it causes performance decent. In contrast, our CFA solves this problem, the results are in the 3rd line of Table 4. The CFA brings the best performance both higher than not using flipping and directly using flipping, which demonstrates that our CFA can take the advantage of the image flipping augmentation meanwhile eliminate the relationship changes caused by flipping operation.

## References

- [1] Garrick Brazil and Xiaoming Liu. M3d-rpn: Monocular 3d region proposal network for object detection. In *Proceedings of the IEEE/CVF International Conference on Computer Vision*, pages 9287–9296, 2019.
- [2] Xiaozhi Chen, Kaustav Kundu, Ziyu Zhang, Huimin Ma, Sanja Fidler, and Raquel Urtasun. Monocular 3d object de-

- tection for autonomous driving. In *Proceedings of the IEEE Conference on Computer Vision and Pattern Recognition*, pages 2147–2156, 2016.
- [3] Yongjian Chen, Lei Tai, Kai Sun, and Mingyang Li. Monopair: Monocular 3d object detection using pairwise spatial relationships. In *Proceedings of the IEEE/CVF Conference on Computer Vision and Pattern Recognition*, pages 12093–12102, 2020.
  - [4] Kaiwen Duan, Song Bai, Lingxi Xie, Honggang Qi, Qingming Huang, and Qi Tian. Centernet: Keypoint triplets for object detection. In *Proceedings of the IEEE/CVF International Conference on Computer Vision*, pages 6569–6578, 2019.
  - [5] Tong He and Stefano Soatto. Mono3d++: Monocular 3d vehicle detection with two-scale 3d hypotheses and task priors. In *Proceedings of the AAAI Conference on Artificial Intelligence*, volume 33, pages 8409–8416, 2019.
  - [6] Buyu Li, Wanli Ouyang, Lu Sheng, Xingyu Zeng, and Xiaogang Wang. Gs3d: An efficient 3d object detection framework for autonomous driving. In *Proceedings of the IEEE/CVF Conference on Computer Vision and Pattern Recognition*, pages 1019–1028, 2019.
  - [7] Peixuan Li, Huaici Zhao, Pengfei Liu, and Feidao Cao. Rtm3d: Real-time monocular 3d detection from object keypoints for autonomous driving. *arXiv preprint arXiv:2001.03343*, 2, 2020.
  - [8] Lijie Liu, Jiwen Lu, Chunjing Xu, Qi Tian, and Jie Zhou. Deep fitting degree scoring network for monocular 3d object detection. In *Proceedings of the IEEE/CVF Conference on Computer Vision and Pattern Recognition*, pages 1057–1066, 2019.
  - [9] Lijie Liu, Chufan Wu, Jiwen Lu, Lingxi Xie, Jie Zhou, and Qi Tian. Reinforced axial refinement network for monocular 3d object detection. In *European Conference on Computer Vision*, pages 540–556. Springer, 2020.
  - [10] Rosanne Liu, Joel Lehman, Piero Molino, Felipe Petroski Such, Eric Frank, Alex Sergeev, and Jason Yosinski. An intriguing failing of convolutional neural networks and the coordconv solution. *arXiv preprint arXiv:1807.03247*, 2018.
  - [11] Arsalan Mousavian, Dragomir Anguelov, John Flynn, and Jana Kosecka. 3d bounding box estimation using deep learning and geometry. In *Proceedings of the IEEE Conference on Computer Vision and Pattern Recognition*, pages 7074–7082, 2017.
  - [12] Zengyi Qin, Jinglu Wang, and Yan Lu. Monogrnet: A geometric reasoning network for monocular 3d object localization. In *Proceedings of the AAAI Conference on Artificial Intelligence*, volume 33, pages 8851–8858, 2019.
  - [13] Thomas Roddick, Alex Kendall, and Roberto Cipolla. Orthographic feature transform for monocular 3d object detection. *arXiv preprint arXiv:1811.08188*, 2018.
  - [14] Andrea Simonelli, Samuel Rota Buló, Lorenzo Porzi, Manuel López-Antequera, and Peter Kotschieder. Disentangling monocular 3d object detection. In *Proceedings of the IEEE/CVF International Conference on Computer Vision*, pages 1991–1999, 2019.
  - [15] Xingyi Zhou, Dequan Wang, and Philipp Krähenbühl. Objects as points. *arXiv preprint arXiv:1904.07850*, 2019.